Chinese Chemical Letters 37 (2026) 111401

Contents lists available at ScienceDirect

Chinese Chemical Letters

journal homepage: www.elsevier.com/locate/cclet

Black phosphorus nanosheets-based platform for B-cell lymphoma chemo-photothermal therapy

Xiaoyan Liu[a,b,1], Cong Xu[a,1], Ruhe Zhang[a,1], Yilu Zheng[a,1], Hengyu Liu[a], Haolin Chen[c,*], Meng Zhao[a,d,*], Jun Wu[a,e,f,*], Dongjun Lin[a,*]

[a] Department of Hematology, The Seventh Affiliated Hospital, Sun Yat-sen University, Shenzhen 518107, China
[b] Department of Hematology, Sun Yat-sen Memorial Hospital, Sun Yat-sen University, Guangzhou 510120, China
[c] Department of Anesthesiology, General Hospital of Southern Theater Command of PLA, Guangzhou 510010, China
[d] Key Laboratory of Stem Cells and Tissue Engineering (Ministry of Education), Zhongshan School of Medicine, Sun Yat-sen University, Guangzhou 510080, China
[e] Bioscience and Biomedical Engineering Thrust, The Hong Kong University of Science and Technology (Guangzhou), Guangzhou 511400, China
[f] Division of Life Science, The Hong Kong University of Science and Technology, Hong Kong 999077, China

ARTICLE INFO

Article history:
Received 24 March 2025
Revised 27 May 2025
Accepted 29 May 2025
Available online 30 May 2025

Keywords:
Black phosphorus nanosheets
pH/NIR dual-triggered
B-cell lymphoma
Chemotherapy
Photothermal therapy

ABSTRACT

In the treatment of B-cell lymphoma, chemotherapy as a monotherapy encounters significant challenges like drug resistance, side effects, and limited cytotoxicity. A novel strategy combining chemotherapy and photothermal therapy uses nanomaterials to convert light into heat, locally heating tumor tissues to induce thermal ablation while enhancing the effectiveness of chemotherapeutic agents and reducing toxic side effects on normal cells. Here, we developed a multifunctional black phosphorus nanosheets (BP NSs) for chemo-photothermal synergistic therapy of lymphoma. BP NSs were synthesized from bulk black phosphorus crystal powders utilizing a modified liquid exfoliation technique and functionalized with polyethylene glycol (PEG) to improve stability. The PEGylated BP NSs were loaded with two chemotherapeutic agents, gemcitabine (Gem) and doxorubicin (DOX), forming GD-BP@PEG NSs. The nanosheets exhibit excellent physical stability, efficient photothermal conversion, and pH/near-infrared (NIR) dual-responsive drug release. *In vitro* cell experiments demonstrated that GD-BP@PEG NSs significantly increased cytotoxicity and apoptosis, especially with NIR laser irradiation. Furthermore, *in vivo* studies in A20 lymphoma-bearing BALB/c nude mice revealed GD-BP@PEG NSs passively accumulated with high concentrations at the tumor site, efficiently inhibiting lymphoma growth with minimal systemic toxicity, demonstrating significant advantages over single treatments of chemotherapy or photothermal therapy alone. In summary, this pH/NIR dual-triggered BP NSs system could serve as a promising nanoplatform for chemo-photothermal synergistic treatment of B-cell lymphoma.

© 2026 Published by Elsevier B.V. on behalf of Chinese Chemical Society and Institute of Materia Medica, Chinese Academy of Medical Sciences.

Lymphoma is the fourth most common cancer globally, with high morbidity and mortality rates. Diffuse large B-cell lymphoma, with an estimated 150,000 new cases diagnosed annually, is the most common subtype of lymphoma [1,2]. Currently, chemotherapy is the primary treatment method for B-cell lymphoma [3]. Doxorubicin (DOX), a broad-spectrum antitumor agent, inhibits the proliferation of tumor cells by intercalation with DNA, showing efficacy against hematological malignancies and various solid tumors [4]. However, DOX has significant side effects, including short half-life, lower bioavailability, and specificity for cancer cells, along with nephrotoxicity, severe myelosuppression, and cardiotoxicity [5,6]. Gemcitabine (Gem), a cytidine nucleoside derivative with anti-tumor activity, is an important part of the treatment regimen for lymphoma [7,8]. Nonetheless, its clinical application has been significantly limited by the poor pharmacokinetic properties, short half-life, unsatisfactory biological distribution in tumor tissues, more toxic side effects, long-term multiple administration, and acquired drug resistance [9]. Therefore, enhancing the distribution of chemotherapy drugs in lymphoma tissues, maximizing their bioavailability, reducing side effects, and exploring treatment modes other than chemotherapy are crucial for improving the treatment effect of lymphoma.

Nano-drug delivery systems (nano-DDSs) have been widely used for the therapy of cancer and other diseases due to their in-

* Corresponding authors.
E-mail addresses: chenhlin8@mail2.sysu.edu.cn (H. Chen), zhaom38@mail.sysu.edu.cn (M. Zhao), junwuhkust@ust.hk (J. Wu), lindj@mail.sysu.edu.cn (D. Lin).
[1] These authors contributed equally to this work.

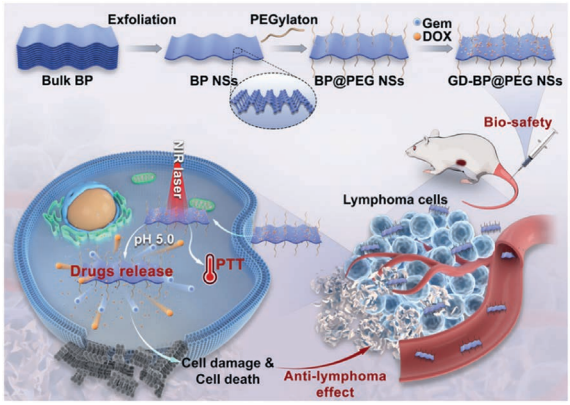
https://doi.org/10.1016/j.cclet.2025.111401
1001-8417/© 2026 Published by Elsevier B.V. on behalf of Chinese Chemical Society and Institute of Materia Medica, Chinese Academy of Medical Sciences.

herent advantages, such as improved drug stability and solubility, minimized side effects, extended circulation time, targeted delivery to specific tissues, and enhanced cellular uptake [10–14]. In recent years, nanomaterial-mediated photothermal therapy (PTT) has attracted significant interest due to its high efficiency, minimal invasiveness, low cost, reduced tissue damage, and low systemic cytotoxicity [15,16]. By utilizing nano-DDSs to combine chemotherapy with PTT, it is possible to effectively target the tumor sites, minimize drug loss, enhance cellular uptake, and improve the chemotherapy efficacy [17]. Additionally, by adjusting the intensity of the external laser irradiation to precisely kill tumor cells, thereby improving treatment efficiency, and reducing the risk of tumor recurrence [18].

Black phosphorus nanosheets (BP NSs), are a new type of two-dimensional nanomaterial with adjustable layer-dependent bandgaps (0.3–2.0 eV) [19], high surface-to-volume ratio, and great absorption in the visible and near-infrared (NIR) region. It has shown great potential in biomedical fields such as bioimaging [20], antibacterial uses [21], drug/gene delivery [22], photodynamic therapy [23], and PTT [24]. Additionally, the major degradation product of BP NSs is phosphate anions [25], which are non-toxic to normal cells but can selectively induce tumor cell death [26,27]. At present, the research on the anti-cancer treatment of BP mainly focuses on solid tumors [24,28,29], especially breast cancer, but its application in hematological malignancies has been minimally investigated.

In this study, we synthesized BP NSs from black phosphorus crystal powders employing a modified liquid exfoliation technique with tip ultrasonic methods and functionalized with positively charged polyethylene glycol (PEG) through electrostatic adsorption. The PEGylated BP NSs effectively loaded two chemotherapeutic drugs, Gem, and DOX, constructing a GD-BP@PEG NSs. PEG coating enhances the stability of the BP NSs, prolongs the circulation time *in vivo*, and increases the uptake by lymphoma cells. Furthermore, GD-BP@PEG NSs exhibit pH/NIR dual-triggered drug release and photothermal activity, demonstrating significantly better anti-lymphoma efficacy *in vitro* and *in vivo* compared to chemotherapy or PTT alone, indicating their potential as a promising nanoplatform for combined chemotherapy and PTT.

First, the synthesis process of the GD-BP@PEG NSs is illustrated in Scheme 1. In this study, the modified liquid exfoliation technique with ultrasonication, as described in the previous study [30], was used to prepare BP NSs from BP powder in *N*-methyl-2-pyrrolidone (NMP). As observed by transmission electron microscope (TEM), the lateral diameter of BP NSs was approximately 165 nm (Fig. 1A). Dynamic light scattering (DLS) results indicated that the average diameter of the BP NSs was 176 ± 15 nm,



Scheme 1. Schematic illustration of the construction of GD-BP@PEG NSs and its application in combined chemo-photothermal therapy for lymphoma.

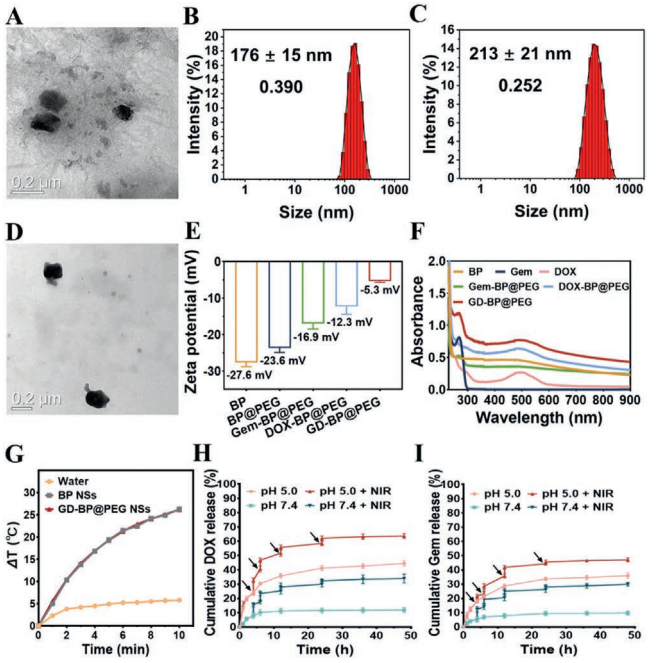


Fig. 1. (A) TEM image of BP NSs. The size distribution of (B) BP NSs and (C) GD-BP@PEG NSs. (D) TEM image of GD-BP@PEG NSs. (E) Zeta potential measurements of different NSs. (F) UV–vis-NIR absorption spectra of different NSs. (G) Photothermal heating curves of BP NSs and GD-BP@PEG NSs suspension (100 μg/mL of BP NSs equivalent, 808 nm, 1.5 W/cm^2, 10 min). *In vitro* (H) DOX and (I) Gem release profile from GD-BP@PEG NSs in pH 7.4 and 5.0 media, (808 nm, 1.5 W/cm^2, 5 min) indicated. Data are presented as mean ± standard deviation (SD) ($n = 3$).

with a uniform distribution (Fig. 1B). However, BP NSs exhibit poor stability under physiological conditions, making them prone to degradation in the presence of oxygen and water [31]. The main modification strategies have been developed to enhance the stability of BP NSs include electrostatic interactions with functionalized components, and covalent conjugation *via* chemical bonds such as covalent bonds, coordinate bonds and π-bonding [31,32]. Commonly used modification materials typically alter the surface charge through amino groups (-NH_2) or enable further chemical functionalization. Notably, amino-based modifications, particularly PEG-NH_2, have emerged as the most extensively studied strategies for BP NSs stabilization [31]. Based on these findings, we selected PEGylation to modify BP NSs to enhance their stability in a physiological medium [33]. Although violet phosphorus (VP) shows better environmental stability than BP NSs [34], we chose BP NSs as the carrier material in this study due to its more established biomedical applications and superior photothermal properties. The narrower bandgap of BP NSs enables stronger NIR absorption and higher photothermal conversion efficiency, making it particularly effective for deep-tissue applications, while its well-characterized surface modification strategies and cost-effective production further support its practical implementation [35].

Zhang *et al.* [36] reported that mitoxantrone (MTX) absorbed onto BP NSs *via* electrostatic interaction, and the synthesized MTX@BP NSs showed significant effect in inhibiting breast cancer tumor growth, which was significantly superior to chemotherapy with MTX alone. Therefore, we evaluated BP@PEG NSs as a therapeutic delivery platform. First, Gem and DOX were mixed with BP@PEG NSs solution in different ratios (the mass ratios of Gem and DOX to BP NSs were 0.5, 1, 2, 3, and 4, respectively), stirred overnight and then removed excess free Gem or DOX molecules, the drug loading rate of BP@PEG NSs was measured by the ultraviolet-visible (UV–vis) spectra. The results indicated that the drug loading capacity increased linearly with rising

concentrations of Gem/BP and DOX/BP (Figs. S1A and B in Supporting information). Finally, a mass ratio of BP:Gem:DOX = 1:3:2 was selected to prepare GD-BP@PEG NSs. The encapsulation efficiency (EE) was determined to be 86.18 % for DOX and 10.35 % for Gem. DOX and Gem were adsorbed to the wavy surface of BP NSs through non-covalent bonds. Numerous studies have confirmed that nanoparticles within a size range of 20–200 nm possess an enhanced permeability and retention (EPR) effect within tumor tissues, which can effectively avoid premature clearance by the kidneys and ensure a high drug loading rate [37,38]. As shown in Figs. 1C and D, the thickness of BP NSs increased and the surface became rougher after loading with the drugs DOX and Gem, and the particle size of GD-BP@PEG NSs measured by DLS was approximately 213 ± 21 nm. In general, encapsulating chemotherapy drugs within nano-carriers can change their entry mechanism into cancer cells, shifting from passive diffusion to active endocytosis, which enhances drug utilization while potentially reducing side effects on normal cells [39].

After PEG modification, the zeta potential of BP NSs increased from −27.6 mV to −23.6 mV, and after loading with Gem and DOX, the zeta potential further increased to −5.3 mV (Fig. 1E), which demonstrated the successful preparation of GD-BP@PEG NSs. As shown in UV–vis-NIR absorption spectra result, BP NSs exhibited strong absorption bands throughout the UV to NIR regions, with absorption intensity gradually increasing as concentration increased (Fig. S1C in Supporting information). Fig. 1F demonstrated the changes in UV–vis-NIR absorption spectra of BP NSs before and after loading with Gem and DOX. Free Gem has obvious absorption at 267 nm, while free DOX shows absorption at 490 nm. Characteristic peaks in GD-BP@PEG NSs had a slight red shift from 267 nm to 268 nm and 490 nm to 493 nm, verifying interactions between the drugs and BP NSs [40]. Changes in size, charge reversal, and characteristic variations in UV–vis-NIR absorption spectra suggested that Gem and DOX had been successfully loaded onto BP NSs. Additionally, Figs. S2A and B (Supporting information) showed no significant changes in size and polydispersity index (PDI) of GD-BP@PEG NSs within 7 days, indicating that it has high structural stability.

BP NSs exhibit broad NIR absorption across the visible light spectrum and efficiently convert light into localized heat, making them ideal for PTT to induce thermal ablation of tumor cells and cell death [41]. Initially, we measured temperature changes in BP NSs and GD-BP@PEG NSs suspensions under 808 nm NIR laser irradiation to assess their photothermal effects. Both BP NSs and GD-BP@PEG NSs (100 μg/mL, 1.5 W/cm^2) demonstrated a temperature increase of ∼26.2 °C under identical conditions, while pure water raised by only about 5.8 °C (Fig. 1G). This indicates that BP NSs can effectively convert NIR laser energy into thermal energy with minimal impact from surface modifications of Gem and DOX on their photothermal properties. Fig. S3A (Supporting information) demonstrated that the synthesized GD-BP@PEG NSs maintained their peak temperature even after five laser irradiation cycles, suggesting excellent thermal stability. The temperature change curves of GD-BP@PEG NSs solutions at varying concentrations (10–200 μg/mL) under laser irradiation (808 nm, 1.5 W/cm^2) were examined (Fig. S3B in Supporting information). Even at a very low concentration (10 μg/mL), the solution achieved a temperature rise of ∼11.0 °C after 10 min of laser exposure. Besides, the temperature of the GD-BP@PEG NSs aqueous solution significantly raised with higher laser power (0.5–2.0 W/cm^2) (Fig. S3C in Supporting information). Moreover, there were no significant changes in the UV–vis-NIR absorption spectrum of GD-BP@PEG NSs following 808 nm laser exposure (Figs. S4A and B in Supporting information), further affirming their outstanding light stability. The photothermal conversion efficiency (η) was calculated to be 28.0 % (Fig. S5 in Supporting information).

Next, we evaluated the drug release behaviors of GD-BP@PEG NSs under conditions of pH 7.4, 6.8 and 5.0, with or without NIR laser irradiation. As the release curve of DOX shown in Fig. 1H and Fig. S6 (Supporting information), approximately 44 % of DOX was released from GD-BP@PEG NSs within 48 h at pH 5.0, compared to 20.9 % at pH 6.8 and only 11.9 % at pH 7.4. A similar result for Gem was shown in Fig. 1I and Fig. S6 (Supporting information), which also exhibited a faster release rate in the acidic environment of pH 5.0. This enhanced release could be attributed to the protonation of amino groups in the DOX and Gem molecules in an acidic environment, facilitating greater drug release. Additionally, BP NSs gradually degrade in acidic conditions, generating phosphate ions that further increase acidity, promoting drug release from the BP NSs-based delivery system in mildly acidic environments [42]. Given that the tumor microenvironment is typically acidic, the pH-dependent release of DOX and Gem from GD-BP@PEG NSs is advantageous for targeted drug delivery applications in tumors [43], corroborated with similar studies [36,44,45].

Moreover, DOX and Gem also exhibited laser irradiation-dependent release behaviors. As shown in Figs. 1H and I, under both pH 5.0 and 7.4 conditions, the cumulative release of DOX and Gem significantly increased after treated with irradiation (808 nm, 5 min, 1.5 W/cm^2), reaching 63.6 % and 47.1 % after four exposures, respectively. This can be attributed to the photothermal properties of the nanomaterials, which weaken their interaction with the drugs and accelerate drug movement [46]. Concurrently, NIR irradiation causes the composite structure to degrade, further promoting drug release [45]. Therefore, the prepared GD-BP@PEG NSs remain stable under normal physiological conditions but effectively release drugs upon internalization into the weakly acidic tumor environment due to its pH sensitivity and NIR laser exposure, achieving synergistic chemotherapy and photothermal therapy of lymphoma.

The cytotoxicity of layered BP NSs is primarily due to their nanoscale size and layered structure [47]. We evaluated the biocompatibility of BP@PEG NSs using the MTT cytotoxicity assay on A20 cells, human umbilical vein endothelial cells (HUVEC), and HeLa cells (Fig. S7A in Supporting information). The results showed that the relative viability of A20 cells was maintained at 92.6 % even at a high concentration of 100 μg/mL, demonstrating good cell compatibility of BP@PEG NSs. Further investigation revealed the photothermal killing capability of BP@PEG NSs against lymphoma cells (Fig. S7B in Supporting information). Independent NIR laser irradiation had minimal impact on lymphoma cell growth, while BP@PEG NSs exhibited a concentration-dependent photothermal effect. Notably, under 808 nm laser irradiation, 100 μg/mL of BP@PEG NSs induced over 40 % cell death in A20 cells, confirming their efficiency of BP@PEG NSs in PTT. To investigate the cellular internalization mechanism of GD-BP@PEG NSs, we systematically examined their uptake pathways. Nanomaterials typically enter cells *via* three primary endocytic mechanisms: caveolae-dependent endocytosis, clathrin-mediated endocytosis, and macropinocytosis [48]. As shown in Fig. 2A, we employed specific pharmacological inhibitors targeting each pathway: Methyl-β-cyclodextrin (MβCD) for caveolae-mediated uptake, sucrose for clathrin-mediated endocytosis, and amiloride for macropinocytosis [40]. The intracellular fluorescence intensity demonstrated a remarkable reduction in nanosheets uptake only upon amiloride treatment, clearly indicating that GD-BP@PEG NSs predominantly enter cells through macropinocytosis.

For *in vitro* lymphoma treatment, the MTT assay together with live/dead assay was performed to evaluate the therapeutic efficacy of GD-BP@PEG NSs (Figs. 2B and C). A20 cells were exposed to different concentrations of DOX, DOX + Gem, and drug-loaded BP NSs for 24 h. The cytotoxicity of free DOX, DOX + Gem, and drug-loaded BP NSs showed a dose-dependent response. Combination therapy with DOX + Gem demonstrated stronger cytotoxicity compared to

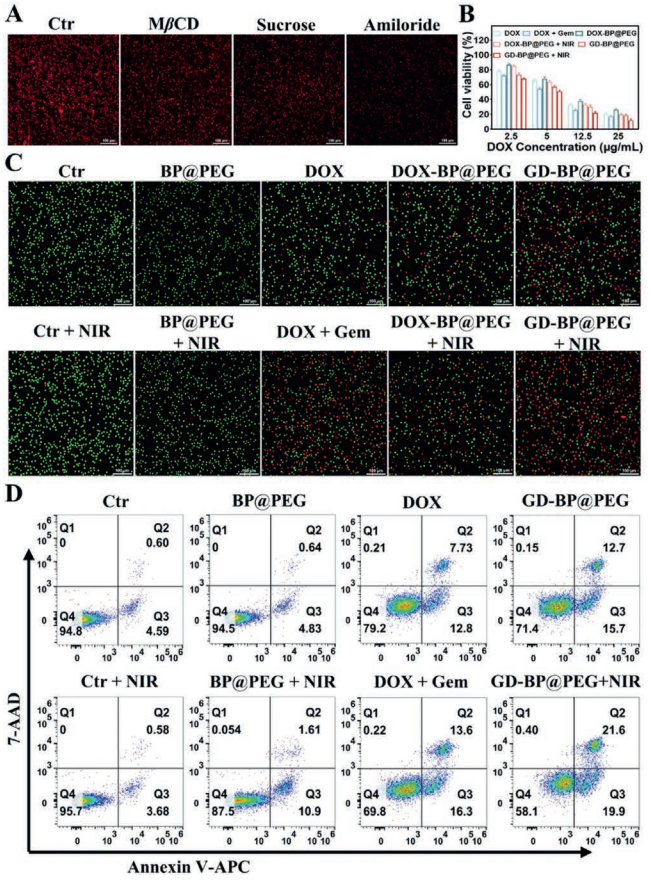


Fig. 2. (A) Mechanism of GD-BP@PEG NSs cellular up taken by A20 cells. (B) Relative viability of A20 cells treated with various concentrations of BP NSs-based platforms compared to DOX alone, and DOX + Gem at the same DOX dose, with or without irradiation. Data are presented as mean ± SD ($n = 3$). (C) Live/dead staining of A20 cells treated with various concentrations of BP NSs-based platforms. Scale bar: 100 μm. (D) Flow cytometric analysis of A20 cells co-stained with Annexin V-APC and 7-AAD. The irradiation condition: 808 nm, 1.5 W/cm^2, 5 min.

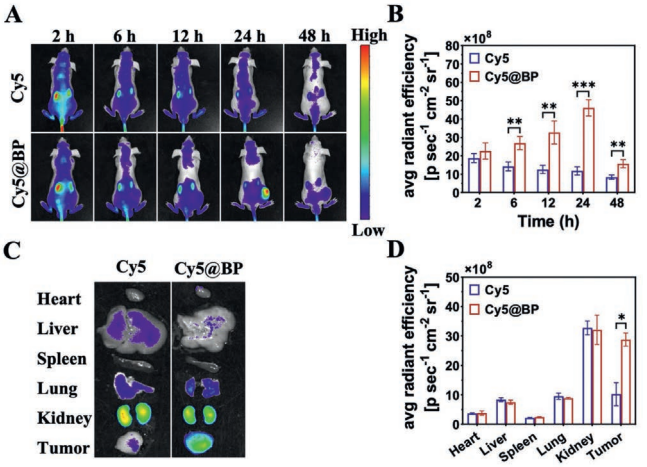


Fig. 3. (A) The biodistribution fluorescence images of free Cy5 and Cy5@BP NSs at different time points. (B) Quantitative analysis of fluorescence intensity statistics of tumor tissues. (C) The fluorescence images and (D) quantitative analysis of major organs and tissues at 48 h. Data are presented as mean ± SD ($n = 3$). $^{*}P < 0.05$, $^{**}P < 0.01$, $^{***}P < 0.001$.

DOX alone, leading to enhanced inhibition rates. While the cytotoxicity of GD-BP@PEG NSs was slightly reduced compared to free DOX + Gem, this may be due to the slower endocytosis mechanism associated with many nanoparticle delivery platforms [28,40,49]. Importantly, after irradiation (808 nm, 1.5 W/cm^2), cells treated with GD-BP@PEG NSs exhibited the lowest survival rate due to the synergistic effects of NIR-triggered photothermal ablation and DNA damage induced by DOX and Gem, indicating the strongest cytotoxic effect from combined chemotherapy and photothermal therapy. The chemo-photothermal combination showed synergistic efficacy (combination index (CI) = 0.83, Chou-Talalay method [50]). Overall, this pH/NIR dual-triggered release mechanism significantly enhanced the anti-lymphoma efficacy of the drugs.

Phototherapy from BP NSs and chemotherapy from DOX and Gem induced apoptosis, which was confirmed by further analysis of Annexin V-allophycocyanin (APC)/7-aminoactinomycin D (7-AAD) staining to demonstrate the anti-lymphoma effects of GD-BP@PEG NSs (Fig. 2D). As shown, without NIR laser irradiation, BP@PEG NSs treatment did not significantly induce apoptosis compared to the control group, with apoptosis rates of 5.47 % and 5.19 %, respectively. However, when cells were exposed to NIR laser irradiation, the apoptosis rate for BP@PEG NSs-treated cells was 12.51 % (with 10.9 % at the early stage and 1.61 % at the late stage). Importantly, under 808 nm laser irradiation, the apoptosis rate for cells treated with GD-BP@PEG NSs reached 41.5 % (with 19.9 % at the early stage and 21.6 % at the late stage), significantly higher than other groups, indicating that combined chemotherapy and photothermal therapy yielded the strongest cytotoxic effects. Quantitative analyses of cell apoptosis are presented in Figs. S8A and B (Supporting information).

To study the *in vivo* biodistribution of BP NSs, the BALB/c nude mice (male, 4–6 weeks) were provided from the Sun Yat-sen University Experimental Animal Center. All animal experiments were approved by the Animal Care and Use Committee of Sun Yat-sen University (approval No. SYSU-IACUC-2024–00239). A lymphoma-bearing mouse model was established by subcutaneously injecting A20 cells for animal experiments. BP NSs were labeled with the fluorescent dye Cy5. Due to the formation of Cy5@BP NSs aggregates, the absorption peak shifted from 640 nm to 645 nm (Fig. S9 in Supporting information). Mice were intravenously injected with free Cy5 or Cy5@BP NSs, and fluorescence imaging was performed at various time intervals to assess the distribution and tumor accumulation of the nanosheets platform *in vivo*. As shown in Figs. 3A and B, both groups of mice exhibited strong systemic blue fluorescence within the first 2 h post-injection, which gradually diminished after 6 h due to dye clearance. Notably, the Cy5@BP NSs group showed higher signals in tumor tissue compared to the free Cy5 group. After 24 h, fluorescence signals in both groups continued to decrease, but strong fluorescence persisted in the tumor tissue of the Cy5@BP NSs group, indicating sustained accumulation of the synthesized nanosheets platform in tumor tissues through the bloodstream, demonstrating EPR effects. All mice were sacrificed after 48 h, and tumors and major organs were collected for fluorescence imaging and quantitative analysis (Figs. 3C and D), revealing intense fluorescence in the tumor tissue of the Cy5@BP NSs group. The fluorescence levels in the heart and spleen were significantly lower than that of other organs, suggesting that BP NSs is easily captured by reticuloendothelial system (RES)-associated organs before renal clearance [51].

Based on the cytotoxic effect of GD-BP@PEG NSs on A20 cells and its passive lymphoma-targeting capability *in vivo*, we further evaluated its anti-lymphoma activity in combination with chemotherapy and photothermal efficacy. As shown in Fig. 4A, when the tumor volume reached 100–150 mm^3, 35 mice were randomly divided into seven groups and administered *via* tail vein injection with saline, BP@PEG NSs, DOX + Gem, and GD-BP@PEG NSs, with a total of five injections (on days 1, 3, 5, 7, and 9). Twenty-four hours after each injection, mice in the laser group received ir-

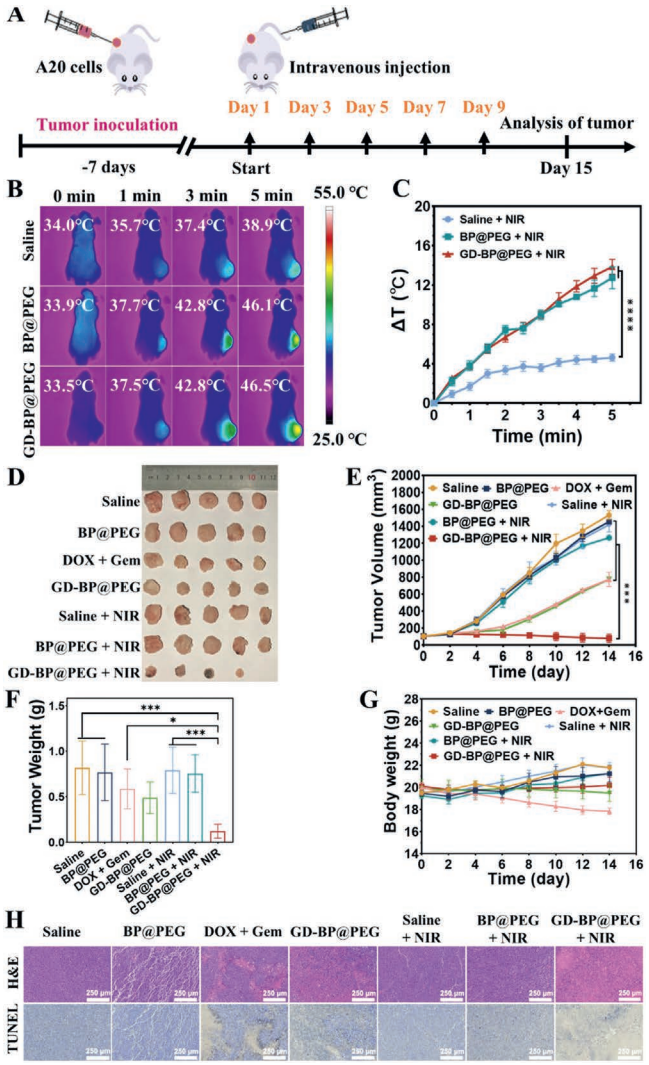


Fig. 4. (A) Schematic illustration of the GD-BP@PEG NSs -induced anti-lymphoma therapy. (B) The IR thermal images of mice after intravenous injection with different formulations for 24 h, followed by exposure to irradiation. (C) Time dependent temperature rise curve under irradiation ($n = 3$). (D) Morphology of tumors of groups. (E) Tumor-growth curves, (F) the average tumor weight, and (G) body weight changes of mice of groups ($n = 5$). (H) H&E staining and TUNEL analysis of lymphoma tissues from various treatment groups. Scale bar: 250 μm. The irradiation condition: 808 nm, 1.5 W/cm^2, 5 min. Data are presented as mean ± SD. $^{***}P < 0.001$, $^{****}P < 0.0001$.

radiation (808 nm, 1.5 W/cm^2, 5 min) at the tumor site. On day 15, all groups of mice were euthanized for analysis. To monitor the *in vivo* photothermal effect, an infrared thermal camera tracked real-time infrared thermal images and temperature changes at the tumor site (Figs. 4B and C). Notably, under 808 nm laser irradiation, local tumor temperatures in mice injected with BP@PEG NSs or GD-BP@PEG NSs rapidly increased to 46.1 and 46.5 °C, respectively. These temperatures are conducive to effective tumor ablation [36]. In comparison, the tumor temperature in the saline group showed a slight increase, indicating that cancer cells remained intact.

By monitoring tumor growth, we further assessed the efficacy of GD-BP@PEG NSs in combination with PTT. The photograph of the tumor tissues and the tumor volume change curve during treatment and was shown in Figs. 4D and E, respectively. The individual tumor growth curves of different treatment groups were shown in Fig. S10 (Supporting information). Saline and saline + NIR groups exhibited rapid tumor growth, indicating that NIR laser irradiation showed minimal effect on tumor growth rate. BP@PEG NSs without irradiation only slightly suppressed lymphoma growth, likely due to the inherent anticancer activity of BP NSs, which may involve high uptake and rapid degradation of BP NSs within cells, leading to a transient increase in cytoplasmic phosphate anion levels, thus inducing G2/M-phase arrest followed by apoptosis and autophagy-mediated death of tumor cells [26]. After laser irradiation, the tumor volume in the BP@PEG NS group rapidly decreased in the initial days, but then grew slowly, indicating insufficient suppression. In contrast, the GD-BP@PEG NSs + NIR treatment group significantly inhibited lymphoma growth, attributed to the EPR effect leading to greater accumulation of NSs in lymphoma tissues, while the heat generated by NIR irradiation effectively killed lymphoma cells and facilitated the release of DOX and Gem from the BP NSs carrier. Fig. 4F and Fig. S11 (Supporting information) showed the average tumor weight and relative tumor weight in different groups, with the residual tumor tissue in the GD-BP@PEG NSs + NIR group significantly smaller than in other groups. These results indicate that the combination of GD-BP@PEG NSs and NIR irradiation has outstanding efficacy in chemotherapy and photothermal therapy.

After 14 days of treatment, hematoxylin and eosin (H&E) and TdT-mediated dUTP nick-end Labeling (TUNEL) staining analyses were performed on the tumor tissues (Fig. 4H). The control group showed tightly arranged tumor cells with no obvious fragmentation, while other treatment groups exhibited varying degrees of nuclear dissolution, necrosis, and fragmentation. In contrast, the GD-BP@PEG NSs + NIR laser treatment group showed significant symptoms of nuclear membrane dissolution, severe necrosis, and nucleolus disappearance, with almost no visible viable lymphoma cells, indicating remarkable therapeutic effects. Furthermore, TUNEL assay results revealed that the saline group showed no significant apoptosis in lymphoma cells, whereas the GD-BP@PEG NSs and GD-BP@PEG NSs + NIR treatment groups exhibited varying degrees of therapeutic effects, with the GD-BP@PEG NSs + NIR group demonstrating the strongest lymphoma-killing effect. Thus, GD-BP@PEG NSs hold great promise for applications in chemo-photothermal synergistic therapy.

In assessing potential *in vivo* toxicity, aside from the DOX + Gem group, which experienced a slight weight loss due to the combined chemotherapy side effects, other groups maintained a slight upward trend (Fig. 4G). H&E staining images of major organs (Fig. S12 in Supporting information) also showed no significant abnormalities, indicating that the application of BP NSs-based nanoplatform is relatively safe. Blood count and serum biochemical indicators (alanine aminotransferase (ALT), aspartate aminotransferase (AST), alkaline phosphatase (ALP), blood urea nitrogen (BUN), creatine kinase (CK), creatinine (CREA), white blood cell (WBC), hemoglobin (HGB), and platelet (PLT)) were measured to assess long-term toxicity. The blood parameters and biochemical indicators of the BP NSs and GD-BP@PEG NSs groups were not significantly different from those of the control group, indicating that BP NSs and GD-BP@PEG NSs do not exhibit significant bone marrow suppression or liver and kidney toxicity (Fig. S13 in Supporting information). However, compared to the control group, mice receiving the DOX + Gem combination chemotherapy showed significantly elevated levels of ALT and AST ($P < 0.0001$), suggesting potential drug-induced liver damage. Additionally, WBC in the DOX + Gem treated group showed significantly lower than in the control group ($P < 0.05$), possibly related to drug-induced bone marrow suppression. These results indicate that GD-BP@PEG NSs offer better biosafety and effectively reduce systemic toxic side effects of DOX + Gem.

In summary, we have developed a novel multifunctional drug delivery nanoplatform, GD-BP@PEG NSs, for the combined chemotherapeutic and photothermal treatment of lymphoma. This nanoplatform demonstrates good stability, with drug release exper-

iments confirming its pH-responsive and NIR radiation-triggered drug release characteristics. Importantly, both *in vitro* and *in vivo* results confirm that GD-BP@PEG NSs exhibit significantly superior anti-lymphoma activity compared to chemotherapy or photothermal treatment alone while having lower side effects. Thus, GD-BP@PEG NSs may serve as a promising strategy for combined chemotherapeutic and photothermal therapy.

Declaration of competing interest

The authors declare that they have no known competing financial interests or personal relationships that could have appeared to influence the work reported in this paper.

CRediT authorship contribution statement

Xiaoyan Liu: Writing – review & editing, Writing – original draft, Methodology, Formal analysis, Data curation. **Cong Xu:** Methodology, Formal analysis. **Ruhe Zhang:** Writing – review & editing, Formal analysis, Data curation. **Yilu Zheng:** Writing – original draft, Validation, Project administration. **Hengyu Liu:** Validation, Methodology. **Haolin Chen:** Writing – review & editing, Validation, Supervision, Funding acquisition, Conceptualization. **Meng Zhao:** Writing – review & editing, Visualization, Validation, Formal analysis, Conceptualization. **Jun Wu:** Writing – review & editing, Validation, Supervision, Funding acquisition, Formal analysis, Conceptualization. **Dongjun Lin:** Writing – review & editing, Validation, Supervision, Funding acquisition, Conceptualization.

Acknowledgments

This project was supported by the National Natural Science Foundation of China (Nos. 52173150, 82270176), the Guangzhou Science and Technology Program City-University Joint Funding Project (Nos. 2024A03J0604, 2023A03J0001), the Science and Technology Program of Guangzhou (No. 2024A04J4558), and Research Start-up Fund of Post-doctoral of SAHSYSU (No. ZSQYRSFPD0074). We sincerely acknowledge the funding and generous support from these foundations.

Supplementary materials

Supplementary material associated with this article can be found, in the online version, at doi:10.1016/j.cclet.2025.111401.

References

[1] D. Ennishi, E.D. Hsi, C. Steidl, et al., Cancer Discov. 10 (2020) 1267–1281.
[2] L.H. Sehn, G. Salles, N. Engl. J. Med. 384 (2021) 842–858.
[3] T. Melchardt, A. Egle, R. Greil, ESMO Open 8 (2023) 100750.
[4] S. Peter, S. Alven, R.B. Maseko, et al., Molecules 27 (2022) 4478.
[5] X. Li, Environ. Res. 234 (2023) 116504.
[6] J.R. Lakkakula, P. Gujarathi, P. Pansare, et al., Carbohydr. Polym. 259 (2021) 117696.
[7] J.S. Abramson, M. Ku, M. Hertzberg, et al., Lancet 404 (2024) 1940–1954.
[8] M. Kamdar, S.R. Solomon, J. Arnason, et al., Lancet 399 (2022) 2294–2308.
[9] W. Zhong, X. Zhang, X. Duan, et al., Acta Biomater. 144 (2022) 67–80.
[10] A. Bisht, D. Avinash, K.K. Sahu, et al., Drug Deliv. Transl. Res. 15 (2025) 102–133.
[11] S. Paroha, J. Verma, R.D. Dubey, et al., Int. J. Pharm. 592 (2021) 120043.
[12] Z. Guo, J. Ye, X. Cheng, et al., Biomater. Res. 28 (2024) 15.
[13] S. Liu, M. Yang, H. Liu, et al., Wiley Interdiscip. Rev. Nanomed. Nanobiotechnol. 16 (2024) e2008.
[14] S. Zhang, Y. Zhang, W. Wang, et al., Chin. Chem. Lett. 35 (2024) 109658.
[15] M. Shi, X. Liu, W. Pan, et al., J. Mat. Chem. B 11 (2023) 6478–6490.
[16] J. Li, W. Zhang, W. Ji, et al., J. Mat. Chem. B 9 (2021) 7909–7926.
[17] Z. Deng, C. Jiang, M.R. Younis, et al., Chin. Chem. Lett. 32 (2021) 2411–2414.
[18] X. Cao, C. Yang, X. Zhu, et al., Chin. Chem. Lett. 35 (2024) 109199.
[19] W. Tao, X. Zhu, X. Yu, et al., Adv. Mater. 29 (2017) 1603276.
[20] M. Huang, Z. Gu, J. Zhang, et al., J. Mat. Chem. B 9 (2021) 5195–5220.
[21] Y. Xu, S. Chen, Y. Zhang, et al., J. Mat. Chem. B 11 (2023) 7069–7093.
[22] L. Qin, S. Jiang, H. He, et al., J. Control. Release 318 (2020) 50–66.
[23] X. Zhang, J. Tang, C. Li, et al., Bioact. Mater. 6 (2021) 472–489.
[24] Y. Zhang, Y. Tian, X. Sheng, et al., Chin. Chem. Lett. 36 (2025) 110193.
[25] T. Zhang, Y. Wan, H. Xie, et al., J. Am. Chem. Soc. 140 (2018) 7561–7567.
[26] W. Zhou, T. Pan, H. Cui, et al., Angew. Chem. Int. Ed. 58 (2019) 769–774.
[27] C. Ma, J. Zhang, Y. Zhang, et al., Chin. Chem. Lett. 32 (2021) 1550–1554.
[28] L. Gao, R. Teng, S. Zhang, et al., Front. Bioeng. Biotechnol. 8 (2020) 769.
[29] H. Chen, Z. Liu, O. Jiang, et al., Giant 8 (2021) 100073.
[30] W. Chen, J. Ouyang, X. Yi, et al., Adv. Mater. 30 (2018) 1703458.
[31] W. Liu, A. Dong, B. Wang, et al., Adv. Sci. 8 (2021) 2003033.
[32] G. Liu, H. Tsai, X. Zeng, et al., Chem. Eng. J. 375 (2019) 121917.
[33] X. Yang, D. Wang, Y. Shi, et al., ACS Appl. Mater. Interfaces 10 (2018) 12431–12440.
[34] H. Zhang, Y. Zhang, Y. Zhang, et al., Nat. Commun. 15 (2024) 6783.
[35] Y. Mei, Y. Cao, W. Wang, Adv. Healthc. Mater. 14 (2025) e2403576.
[36] F. Zhang, F. Peng, L. Qin, et al., Colloid Surf. B: Biointerfaces 180 (2019) 353–361.
[37] S. Shekhar, M. Chauhan, Sonali, et al., Nanomedicine 17 (2022) 1213–1216.
[38] Z. Pei, S. Hu, H. Wei, et al., Chin. Chem. Lett. 37 (2026) 110981.
[39] F.U. Din, W. Aman, I. Ullah, et al., Int. J. Nanomed. 12 (2017) 7291–7309.
[40] W. Chen, J. Ouyang, H. Liu, et al., Adv. Mater. 29 (2017) 1603864.
[41] H. Fu, Z. Li, H. Xie, et al., RSC Adv. 7 (2017) 14618–14624.
[42] L. Chen, C. Chen, W. Chen, et al., ACS Appl. Mater. Interfaces 10 (2018) 21137–21148.
[43] B. Guo, J. Zhao, C. Wu, et al., Colloid Surf. B: Biointerfaces 177 (2019) 346–355.
[44] N. Gao, J. Nie, H. Wang, et al., J. Biomed. Nanotechnol. 14 (2018) 1883–1897.
[45] X. Zeng, M. Luo, G. Liu, et al., Adv. Sci. 5 (2018) 1800510.
[46] L. Shao, R. Zhang, J. Lu, et al., ACS Appl. Mater. Interfaces 9 (2017) 1226–1236.
[47] X. Zhang, Z. Zhang, S. Zhang, et al., Small 13 (2017) 1701210.
[48] S.D. Conner, S.L. Schmid, Nature 422 (2003) 37–44.
[49] A. Li, S. Wang, Z. Zhang, et al., J. Mat. Chem. B 10 (2022) 5191–5202.
[50] T.C. Chou, Pharmacol. Rev. 58 (2006) 621–681.
[51] S. Xiong, Z. Li, Y. Liu, et al., Biomaterials 260 (2020) 120339.